



# Terahertz three-dimensional monitoring of nanoparticle-assisted laser tissue soldering

JUNLIANG DONG,<sup>1,6</sup>  HOLGER BREITENBORN,<sup>1</sup> RICCARDO PICCOLI,<sup>1</sup> LUCAS V. BESTEIRO,<sup>1,2</sup> PEI YOU,<sup>1</sup> DIEGO CARAFFINI,<sup>1</sup> ZHIMING M. WANG,<sup>2</sup> ALEXANDER O. GOVOROV,<sup>2,3</sup> RAFIK NACCACHE,<sup>4,5</sup> FIORENZO VETRONE,<sup>1</sup> LUCA RAZZARI,<sup>1</sup> AND ROBERTO MORANDOTTI<sup>1,2,7</sup> 

<sup>1</sup>*Institut National de la Recherche Scientifique (INRS), Centre Énergie, Matériaux et Télécommunications (EMT), Varennes, QC J3X 1S2, Canada*

<sup>2</sup>*Institute of Fundamental and Frontier Sciences, University of Electronic Science and Technology of China, Chengdu 610054, Sichuan, China*

<sup>3</sup>*Department of Physics and Astronomy, Ohio University, Athens, Ohio 45701, USA*

<sup>4</sup>*Department of Chemistry and Biochemistry and Centre for NanoScience Research, Concordia University, Montreal, QC H4B 1R6, Canada*

<sup>5</sup>*Quebec Centre for Advanced Materials, Department of Chemistry and Biochemistry, Concordia University, Montreal, QC H4B 1R6, Canada*

<sup>6</sup>*junliang.dong@emt.inrs.ca*

<sup>7</sup>*morandotti@emt.inrs.ca*

**Abstract:** In view of minimally-invasive clinical interventions, laser tissue soldering assisted by plasmonic nanoparticles is emerging as an appealing concept in surgical medicine, holding the promise of surgeries without sutures. Rigorous monitoring of the plasmonically-heated solder and the underlying tissue is crucial for optimizing the soldering bonding strength and minimizing the photothermal damage. To this end, we propose a non-invasive, non-contact, and non-ionizing modality for monitoring nanoparticle-assisted laser-tissue interaction and visualizing the localized photothermal damage, by taking advantage of the unique sensitivity of terahertz radiation to the hydration level of biological tissue. We demonstrate that terahertz radiation can be employed as a versatile tool to reveal the thermally-affected evolution in tissue, and to quantitatively characterize the photothermal damage induced by nanoparticle-assisted laser tissue soldering in three dimensions. Our approach can be easily extended and applied across a broad range of clinical applications involving laser-tissue interaction, such as laser ablation and photothermal therapies.

© 2020 Optical Society of America under the terms of the [OSA Open Access Publishing Agreement](#)

## 1. Introduction

Emerging light-based technologies have permeated many aspects of modern medicine, including medical imaging, diagnosis, therapy, and surgery [1]. In particular, among those, laser tissue soldering is an advanced suture-less surgery method for wound healing. The basic principle is to use laser light in combination with a solder material, such as albumin, to “stitch” surface wound cuts together. When the laser light illuminates the applied solder, the underlying tissue heats up and a continuous bond is created, reconnecting collagen [2]. The result is a waterproof seal along the entire wound, which prevents access to external pathogens and does not require suture removal. Advantages of laser tissue soldering over conventional sutures are a less inflammatory response of the tissue, a reduced chance of post-surgery infection, and no allergic reactions to foreign materials being introduced via traditional stitches [3]. Moreover, the laser-assisted wound sealing is less traumatic and retains significantly less scared tissue. It is also faster and easier to apply, while being less skill dependent. Additionally, laser tissue soldering can be used to seal

and connect complex and delicate tissues, including cornea [4], blood vessels [5], and nerves [6], that would be otherwise damaged by conventional suturing.

Recent studies have shown that the soldering process can be enhanced by combining albumin with plasmonic nanoparticles [7–9], such as gold nanorods (GNRs). GNRs, possessing high near-infrared (NIR) absorption cross-sections, can convert light to heat efficiently [10,11]. The GNR-embedded solder solution forms a photo-thermal nanocomposite that facilitates rapid wound sealing with less laser power required (with respect to simple albumin). However, nanoparticle-assisted laser tissue soldering has not been used in the clinical setting yet. The underlying reason is the fact that the rapid elevation in temperature due to laser absorption and the concomitant heat generation can cause significant photothermal tissue damage. Figure 1 schematically illustrates the photothermal reactions that may happen when the laser energy strikes the tissue and is absorbed [12]. The heat generated locally by the incident laser beam is transferred to the adjacent (cooler) areas radially, depending on the thermal conductivity of the tissue; therefore, in this initial stage, the photothermal effect is reversible. If the laser excitation continues, the finite heat conduction of the tissue does not allow for an appropriate transfer of the generated heat; when the local temperature reaches a critical limit ( $\sim 60^\circ\text{C}$ ), coagulation of biomolecules takes place, in turn leading to cell death. A further energy accumulation leads to an additional increase in the local temperature, until the water in the tissue reaches the boiling temperature ( $\sim 100^\circ\text{C}$ ). Few seconds after this stage is reached, water evaporates and the soft tissue drastically reduces its volume. With more laser energy deposited, biomolecules, such as proteins, start burning, which causes carbonization on the surface [13]. Therefore, to minimize tissue damage and optimize the bonding strength [14], a rigorous approach to monitoring of the heated solder and the underlying tissue is strictly necessary.

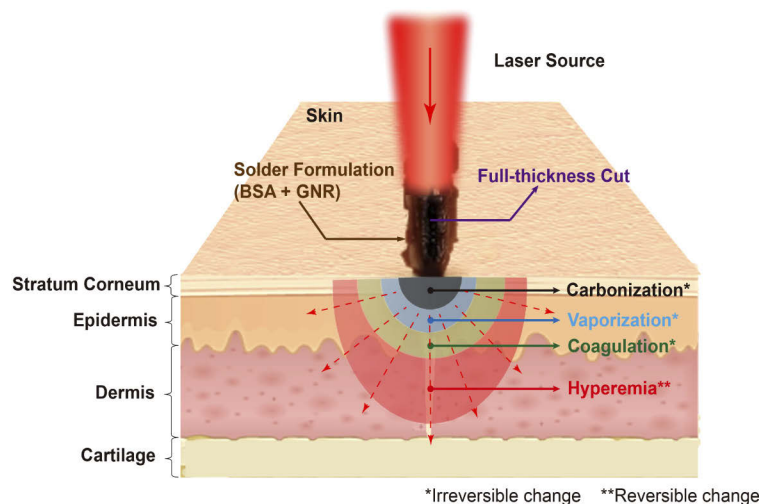


**Fig. 1.** Schematic showing the range of simultaneous photothermal reactions during nanoparticle-assisted laser tissue soldering.

In this work, we capitalize on the unique properties of terahertz (THz) radiation [15] (frequency range between 0.1 and 3 THz in our experiments) to investigate nanoparticle-assisted laser-tissue interaction. We demonstrate, for the first time to our knowledge, the promising capability of the proposed technique to perform simultaneous monitoring of laser-tissue interaction and three-dimensional visualization of the photothermal damage induced by nanoparticle-assisted laser tissue soldering in a non-invasive and non-contact manner. Due to the presence of water in physiological tissues and the extreme absorption of water at THz frequencies, the penetration

depth is limited to only a few hundreds of microns [16]. However, the high sensitivity of THz radiation to water provides easily detectable changes in THz reflectivity for small variations in the tissue hydration level, making the variation of water content an effective contrast mechanism [17,18]. This advantage, together with the low, non-ionizing photon energy [19] (0.4-40 meV) make THz radiation an ideal diagnostic tool for *in-vivo* imaging of skin burns [20,21], melanoma/carcinoma [22,23], breast cancers [24], corneal pathologies [25], as well as diabetic deterioration [26,27]. This study is organized as follows: First, a numerical finite element model is established to qualitatively investigate the spatio-temporal heat transfer and the resulting temperature distribution in skin upon laser illumination. Second, a dynamic THz single-point measurement is conducted to monitor the process of nanoparticle-assisted laser-tissue interaction. The evolution of the THz signals associated with the growth of the photothermal damage is revealed, analyzed, and discussed. Finally, *in-vitro* THz reflective imaging is performed to evaluate the soldered skin and quantitatively characterize the photothermal damage induced by nanoparticle-assisted laser skin soldering in three dimensions.

## 2. Materials and methods

### 2.1. GNR-embedded solder gel and skin samples

The GNR-embedded solder gel was prepared by dissolving 50% weight by volume concentration of bovine serum albumin (BSA) (Sigma-Aldrich) in a 1:1 mixture of GNR dispersion and deionized water. The GNRs are 41 nm in length and 10 nm in width, with an aspect ratio of 4.1, and feature a localized surface plasmon resonance (LSPR) at 808 nm. The GNR dispersion was purchased from Nanopartz. The optical density per unit thickness, OD, of the GNR dispersion was 100. The resulting solder gel consisted of  $7 \times 10^{10}$  nanoparticles/ml. Porcine ear skin was selected as an *in-vitro* model for human skin, since their histological and physiological properties are almost identical [28], hence porcine skin can be considered as a good surrogate for preclinical studies.

### 2.2. Heat transfer modelling

A finite element model implemented in *COMSOL Multiphysics* was established to qualitatively investigate the time-dependent heat transfer and spatial temperature distribution in skin upon laser illumination. As shown in Fig. 2(a), the sample was modeled as a two-layered structure: the skin was considered as a homogeneous layer, including water and low-loss biological background, with 5 mm thickness and 8 mm radius; the solder gel was treated as a homogeneous mixture of BSA and GNR dispersions with a thickness of 0.2 mm and radius of 8 mm. A continuous-wave (CW) NIR laser beam (wavelength at 800 nm) with a radius of 2.2 mm and intensity of 50 mW/mm<sup>2</sup>, was assumed to impinge onto the top center of the modelled sample. The initial temperature was set at 25 °C.

The thermal transfer properties of the biological tissue in absence of blood circulation are simply described by the heat transfer equation [29], which can be expressed as:

$$\rho C_p \frac{\partial T}{\partial t} + \nabla(-k \nabla T) = Q_{ext}, \quad (1)$$

where  $\rho$  is the density (1321 kg/m<sup>3</sup> for the solder gel [30], 1050 kg/m<sup>3</sup> for the porcine skin [31]), and  $C_p$  is the specific heat capacity (3.4 J/(g·K) for the solder gel [30], 3.6 J/(g·K) for the porcine skin [31]); the second term accounts for thermal diffusion where  $k$  represents the thermal conductivity (0.58 W/(m·K) for the solder gel [30], and 0.5 W/(m·K) for the porcine skin [31]);  $T$  and  $t$  are the temperature and time scale, respectively, while  $Q_{ext}$  represents all the external sources which contribute to the heating. By considering the absorbed part of the

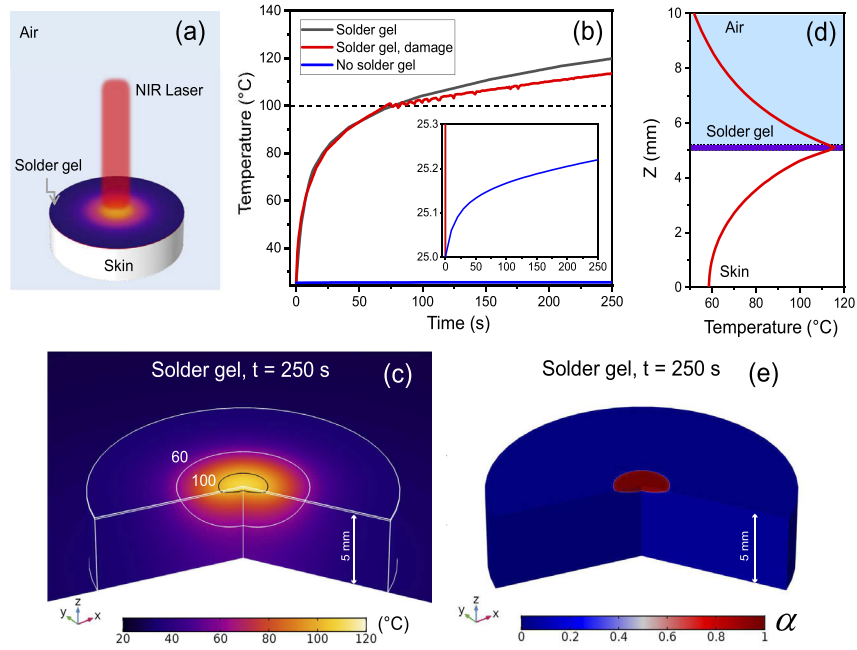


**Fig. 2.** Spatio-temporal heat transfer model of laser-tissue interaction. (a) Schematic diagram of the finite element model of nanoparticle-assisted laser-tissue interaction. (b) Simulated temperature transients at the top center of the skin, with and without modelling the tissue damage. The inset shows the zoom-in of the temperature transient without the application of the solder gel. (c) Simulated three-dimensional temperature distribution in skin with the application of the solder gel after a laser exposure time of 250 s. Temperature contours of 60 °C and 100 °C are highlighted in white and black, respectively. (d) Spatial temperature distribution along the depth direction at the center of the skin sample (at  $t = 250$  s). (e) Estimated damage distribution in skin with the application of the solder gel after a laser exposure time of 250 s.

beam, the laser heat source  $Q_{laser}$  is modeled based on the Beer-Lambert Law in the cylindrical coordinate system as:

$$Q_{laser} = -\left. \frac{\partial I(r, z)}{\partial z} \right|_{abs} = \mu_{abs} I(r, z), \quad (2)$$

$$I(r, z) = I_0(r) e^{-(\mu_{abs} + \mu_{scat})z}, \quad (3)$$

where  $I_0(r)$  is the laser intensity at the surface (with a Gaussian profile, and an average intensity of  $5 \text{ W/cm}^2$ ), while  $\mu_{abs}$  and  $\mu_{scat}$  are the absorption and scattering coefficients of the skin. For the porcine skin, the absorption and scattering coefficients are  $0.02 \text{ cm}^{-1}$  and  $6.5 \text{ cm}^{-1}$  [31], respectively; for the solder gel, the extinction coefficient is  $(\mu_{abs} + \mu_{scat})/\ln 10 = 100 \text{ cm}^{-1}$ , based on the experimental data in which we consider that absorption accounts for 99% of the loss, following the theoretical calculation for the interaction cross-section of GNRs ( $10 \text{ nm} \times 41 \text{ nm}$ ) dominated by absorption. Convection loss  $Q_{conv}$  and radiation loss  $Q_{rad}$  at the surface in contact with the environment are defined as:

$$Q_{conv} = -h(T - T_0), \quad (4)$$

$$Q_{rad} = -\epsilon \sigma (T^4 - T_0^4), \quad (5)$$

where  $h$  is the heat transfer coefficient for convection ( $5 \text{ W/(m}^2 \cdot \text{K)}$ ),  $\epsilon$  is the surface emissivity (0.8), and  $\sigma$  is the Stefan-Boltzmann constant. In hyperthermia processes, tissue necrosis

(permanant damage or death of living tissue) occurs when an excessive amount of energy is absorbed over a certain period of time. Furthermore, we include a simple model to quantify the damage inflicted to the tissue, taking it as occurring when the tissue temperature is elevated above a critical value (100 °C in our case), and maintained for a certain time period  $\tau_{damage}$  (which is chosen as 10 s in our simulation according to our experimental evidence). Therefore, based on a simple model of phase change as an approximation to the necrosis/carbonization of the tissue, the degree of damage can be quantified by a parameter  $\alpha$ , starting at zero (non-damaged tissue) and evolving as:

$$\frac{d\alpha}{dt} = \frac{1}{\tau_{damage}} \theta(T - 100^\circ\text{C}), \quad \theta(x) = \begin{cases} 0, & x < 0 \\ 1, & x \geq 0 \end{cases}, \quad (6)$$

$$Q_{damage} = -L_h \rho \frac{d\alpha}{dt} \theta(\alpha) \theta(1 - \alpha). \quad (7)$$

These equations provide a simple model for quantifying the heat used to drive a phase change process that is characterized by a temperature threshold and a defined time duration. The parameter  $\alpha$  gives an indication of the tissue damage state, and increases from zero as the local temperature reaches the critical value. When it reaches 1, the tissue is considered fully necrotic and carbonized. The fraction of necrotic tissue can be estimated by spatially mapping the quantity  $\min(\alpha, 1)$ . A heat sink is associated with the reaction, to properly model the amount of energy required to realize the burning process, in turn leading to tissue damage. Therefore,  $Q_{damage}$  is calculated from Eq.7, in which the damage enthalpy change  $L_h$  is taken as the enthalpy of water vaporization (2250 kJ/kg). Based on the model outlined above, the heat equation in Eq.1 is solved using *COMSOL Multiphysics*. The temperature distributions with and without the application of the solder gel at each time step were calculated to obtain the simulation results.

### 2.3. THz imaging system

The THz time-domain spectroscopy (TDS) system employed in this study, shown in Fig. 3(a), is based on two photoconductive antennas (PCAs, for THz emission/detection, Tera8-1 from Menlo Systems) with a gap size of 5  $\mu\text{m}$  made of low-temperature-grown gallium arsenide (LT-GaAs). The transmitter is biased with 30 Vpp and modulated by a 1 kHz square wave. Photocarriers within the PCA substrate are excited by a laser source (775 nm wavelength, FemtoFiber Smart from Toptica), which provides 100-fs-long pulses at 100 MHz repetition rate. The main beam is split into a pump and a probe via a 50/50 beam splitter in order to excite the transmitter and detector, respectively. The emitted THz pulse is guided by four polymethylpentene (TPX) lenses (BATOP Optoelectronics) to realize a reflection geometry with a 1.5 mm focusing spot size. The skin sample is placed in the focal plane of the optical setup. The angle of incidence is 45° relative to the normal axis of the sample. The power spectrum of the emitted THz pulses peaks at about 0.3 THz and exceeds 3 THz in bandwidth with a dynamic range of 60 dB. A 50-ps long fast delay line (scanDelay 50 from APE) was used to delay the probe with respect to the pump beam in order to read out a single THz waveform every second. The averaging time constant of the lock-in amplifier was set to 300  $\mu\text{s}$ . The sample was mounted on a motorized translation stage enabling pixel-by-pixel THz raster-scans.

### 2.4. Signal post-processing algorithm

THz frequency-wavelet domain deconvolution (FWDD) [32] was employed to process the recorded THz reflected signals in order to enhance the resolution in depth. In the time domain, the reflected THz signal  $r(t)$  is the convolution of the incident THz pulse  $i(t)$  with the impulse-response function  $h(t)$ , which corresponds to the structure and properties of the sample at a given position [33]. Ideally,  $h(t)$  can be retrieved by the inverse Fourier transform based on the convolution theorem. However, successful deconvolution cannot be expected by directly applying the inverse



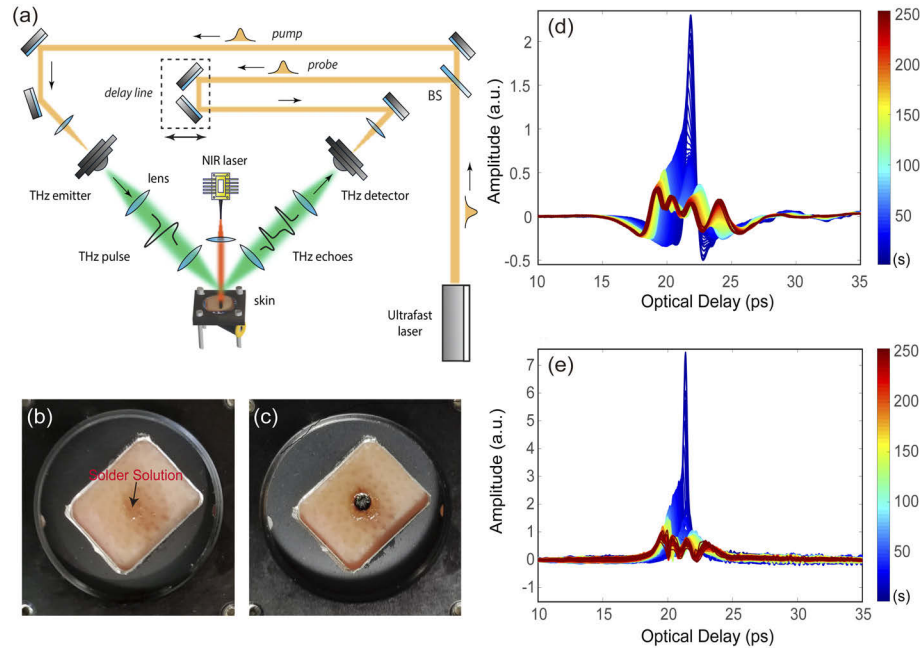


**Fig. 3.** Dynamic THz single-point measurements. (a) Experimental THz-TDS setup in reflection geometry. The 786 nm NIR beam is used to plasmonically heat the GNR-embedded solder gel and the porcine skin sample. (b) Digital photograph of the porcine skin sample with the GNR-embedded solder gel applied on the surface. (c) Digital photograph of the porcine skin sample after plasmonic heating for 250 s. Here, carbonization on the surface is observed. (d) The 250 reflected THz signals recorded (one trace per second) during the laser illumination. (e) The 250 deconvolved signals achieved after applying the FWDD algorithm to the raw THz signals in (d).

Fourier transform, since division by small numbers in the frequency domain will give rise to large spikes in the high frequency region, in turn leading to severe ringing in the time domain. Therefore, frequency-domain filtering is introduced to suppress the high-frequency noise. Then  $h(t)$  can be expressed as:

$$h(t) = FFT^{-1}[FFT(f(t)) \times \frac{FFT(r(t))}{FFT(i(t))}], \quad (8)$$

where  $FFT$  denotes the Fourier transform,  $FFT^{-1}$  the inverse Fourier transform, and  $f(t)$  corresponds to the filter function in the time domain. In this study, a Hanning window function is chosen as the filter function  $f(t)$ , and its frequency spectrum  $F(\omega)$  can be expressed as,

$$F(\omega) = \begin{cases} e^{i\omega t_0} \cos^2(\frac{\omega}{4f_c}), & |\omega| < 2\pi f_c \\ 0, & |\omega| \geq 2\pi f_c \end{cases}, \quad (9)$$

where  $t_0$  corresponds to the arrival time of the THz main peak in time and  $f_c$  is the cut-off frequency. The selection of  $f_c$  is a compromise between the time resolution and frequency-domain filtering. Usually, a relatively high value of  $f_c$  is chosen ( $f_c = 3$  THz in this study) in order to achieve a high resolution in time. However, in this case, a satisfactory signal-to-noise ratio in time cannot be guaranteed. Therefore, stationary wavelet shrinkage is applied to further attenuate the residual noise in time. The *symlet* (sym4) wavelets [34], which are a modified form of *Daubechies*

wavelets, are chosen in this study. A maximum level of 7 is used for the wavelet decomposition as no significant improvement can be observed for higher levels to justify the extra computational expense. Quite often, the signal after FWDD contains slow fluctuations corresponding to the low-frequency noise, due to the THz source being inefficient in the low frequency region. This kind of noise can be cancelled by subtracting the baseline of the deconvolved signal. The resulting deconvolved signal, representing the impulse-response function, provides a new imaging domain with enhanced depth resolution.

### 3. Results and discussions

#### 3.1. Spatio-temporal heat transfer modelling of nanoparticle-assisted laser-tissue interaction

The spatio-temporal temperature distributions were estimated using the heat equation in a simplified model of porcine skin described in the previous section. The temperature transients at the top center of the skin were simulated and displayed in Fig. 2(b). With the application of a GNR-embedded solder gel, the temperature transient quickly increased within 25 s, and gradually saturated thereafter. The achieved temperature in the solder gel could reach 60 °C within only 20 s, and 100 °C within 75 s. Simulated temperature transients with (in red) and without (in black) accounting for the thermal damage model were compared. After the temperature reached 100 °C, some of the absorbed energy was directed to produce tissue damage, therefore, acting like an effective heat sink. On the other hand, if the solder gel was not applied, most of the laser light was scattered by the skin sample and the increase of the temperature was very small, as shown in the inset of Fig. 2(b). The significant increase of temperature in the solder gel is due to the fact that the embedded GNRs (10 nm × 41 nm in size) can absorb most of the beam intensity and convert it efficiently to heat due to their LSPR and the collective heating effect [10]. It is also crucial to mention that the GNRs embedded in the solder gel interact with light through absorption, showing little scattering and, consequently, behaving as excellent nanoheaters. The simulated spatial temperature distribution, following plasmonic heating for 250 s, is depicted in Fig. 2(c). The temperature contours corresponding to 60 °C and 100 °C are highlighted in white and black, respectively. As previously mentioned, a temperature above 60 °C leads to the irreversible coagulation of biomolecules, and water evaporation is dominant when the temperature is higher than 100 °C. The maximum temperature is recorded at the center of the laser beam, due to its Gaussian intensity profile, from which the temperature decays in the radial direction. Importantly, it also decreases in the depth, given that light absorption occurs at the solder gel position and almost not at all within the skin. As shown in Fig. 2(d), the temperature distribution as a function of depth in the center of the skin model demonstrates that the addition of the GNR-embedded solder gel results in a well-confined heat deposition volume in the proximity of the solder-applied region and lessens the outgoing radiative heat flux. Figure 2(e) shows the distribution of the estimated tissue damage by plotting the damage indicator  $\alpha$  ranging from 0 (healthy tissue) to 1 (necrotic tissue). Assuming a temperature threshold of 100 °C, the estimated damage mainly corresponds to the carbonization induced by plasmonic heating.

Summarizing the results of the numerical simulations, we can conclude that the application of the GNR-embedded solder gel results in a significant and rapid temperature increase, as well as a localized heat distribution within the sample. It is noteworthy to mention that the temperature gradient formed during the photothermal process varies the water content as a function of depth, thus producing different zones of thermal damage in skin. In the following section, we show how THz radiation can be utilized to monitor the process of nanoparticle-assisted laser-tissue interaction and characterize various zones featuring different thermal damage in three dimensions.

### 3.2. Dynamic THz investigation of nanoparticle-assisted laser-tissue interaction

To identify the evolution of THz signals during the laser-tissue interaction process, a dynamic THz single-point measurement, relying on the THz-TDS system shown in Fig. 3(a), was performed during plasmonic heating. A thin layer of solder gel was applied onto the fresh porcine skin sample, as presented in Fig. 3(b). A CW NIR laser emitting at 786 nm illuminated on the center of the solder gel with an optical intensity of  $42 \text{ mW/mm}^2$ , activating the strong LSPR of the GNRs within the solder, thus heating the surrounding skin tissue. The NIR laser beam was collimated with a diameter ( $1/e^2$  of the intensity) of 4.4 mm. In this configuration, the heating speed is relatively slow, which in turn allows THz waves to precisely track the process of laser-tissue interaction. The THz beam was focused on the center of the sample with an incident angle of  $45^\circ$  and overlapped with the NIR laser beam. The reflected THz signals were simultaneously recorded at the speed of one trace per second. Plasmonic heating was induced for 250 s and stopped due to carbonization on the sample surface (as predicted via numerical simulations in Fig. 2(e) and shown in Fig. 3(c)), leading to the occurrence of a surface bump, due to rapid water evaporation inside the skin. 250 THz traces were recorded during the THz single-point dynamic measurement as depicted in Fig. 3(d). Two important features of the THz signal evolution can be identified: first, the amplitude of the reflected THz signals decreases drastically. This is due to the heat-induced reduction of water content in the solder gel as well as in the skin, which leads to a lower THz reflectivity and a higher THz penetration. Second, the temporal duration of the THz signals increases gradually. This is because the resulting photothermal damage forms various zones with different refractive indices along the skin depth. THz echoes will occur when THz waves encounter the interfaces between adjacent zones. The overlapping of THz echoes, due to the subwavelength thicknesses of such zones, prolongs the time duration of the THz reflected signals. Therefore, in order to properly characterize the effects of the photothermal damage as a function of depth, the overlapping echoes should be resolved in time.

The 250 recorded THz traces were processed by FWDD, and the resulting deconvolved signals are shown in Fig. 3(e). The peak in the deconvolved signals indicates the existence of an interface within the sample. Specifically, the position and amplitude of the peak corresponds to the location and reflectivity of the interface, respectively, while the sign of the peak depends on the refractive indices of the adjacent layers. In our case, a positive peak corresponds to the reflection when THz waves propagate from a layer with a low refractive index to a layer with a high refractive index. Almost all the signs of the peaks shown in Fig. 3(e) are positive, mainly because THz waves propagate from a low-water-content (i.e., low-refractive-index) zone to a high-water-content (i.e., high-refractive-index) zone.

Typical recorded THz raw and deconvolved signals at specific times  $t$  are selected and plotted in Fig. 4 to investigate the signal evolution during the plasmonic heating process. Note that all the deconvolved signals are normalized to their maximum amplitude. In the beginning, at  $t = 1 \text{ s}$  (i.e. after heating the sample for 1 s), shown in Fig. 4(a1) and (b1), both the raw and deconvolved signals demonstrate that only one THz echo was received, which corresponds to the reflection from the surface of the solder gel. The reflectivity was high and no further THz penetration was observed due to the initial high-water content in the solder gel. As the plasmonic heating started, the temperature elevated rapidly and the water content decreased within the solder gel. Consequently, THz waves were able to pass through the solder and reach the underlying skin surface. Figure 4(a2) shows the THz raw signal at  $t = 20 \text{ s}$ , in which a wider THz pulse with lower amplitude was observed compared to the raw signal at  $t = 1 \text{ s}$ . This wider pulse indicates the existence of overlapping echoes. After FWDD, as shown in Fig. 4(b2), two peaks are clearly identified, corresponding to the reflections from the solder surface and the solder/skin interface. As the heating continued, the solder was solidified and the water content in the skin kept decreasing with depth, enabling more THz penetration into the skin. At  $t = 40 \text{ s}$ , partial overlapping echoes are observed in Fig. 4(a3), where the width of the second peak in the



deconvolved signal in Fig. 4(b3) is larger compared with that at  $t = 20$  s. This is because the heat-induced gradient of the water content formed a gradual interface (from low to high water content), corresponding to the initial region of the coagulation zone in the skin. At  $t = 50$  s, one additional echo occurs as shown in Fig. 4(a4) and, after FWDD, we can clearly identify one additional layer in Fig. 4(b4), which corresponds to the stratum corneum of skin. The stratum corneum was dried out at this stage and was resolved by THz waves. At  $t = 70$  s, burning of the solder as well as of the stratum corneum took place, thus carbonization started to appear on the sample surface. In Fig. 4(a5) and (b5), a weak interface between the carbonized solder and stratum corneum was observed, and the coagulation zone moved towards the epidermis. A further temperature increase led to the formation of a carbonization zone in the epidermis, as shown in Fig. 4(a6) and (b6). As the heating continued, the zones of carbonization and coagulation in the epidermis became larger, as shown in Fig. 4(a7) and (b7). The laser was finally switched off at  $t = 250$  s, because of the observable surface bump. Such occurrence is due to the rapid water evaporation inside the skin, since the water content in the epidermis is much higher than that in the stratum corneum. The deconvolved signal at  $t = 250$  s, shown in Fig. 4(b8), exhibits a negative peak indicating a zone with lower refractive index. This is a consequence of the fact that the carbonized area was detached from the underlying skin forming the bump, thus creating an air gap.

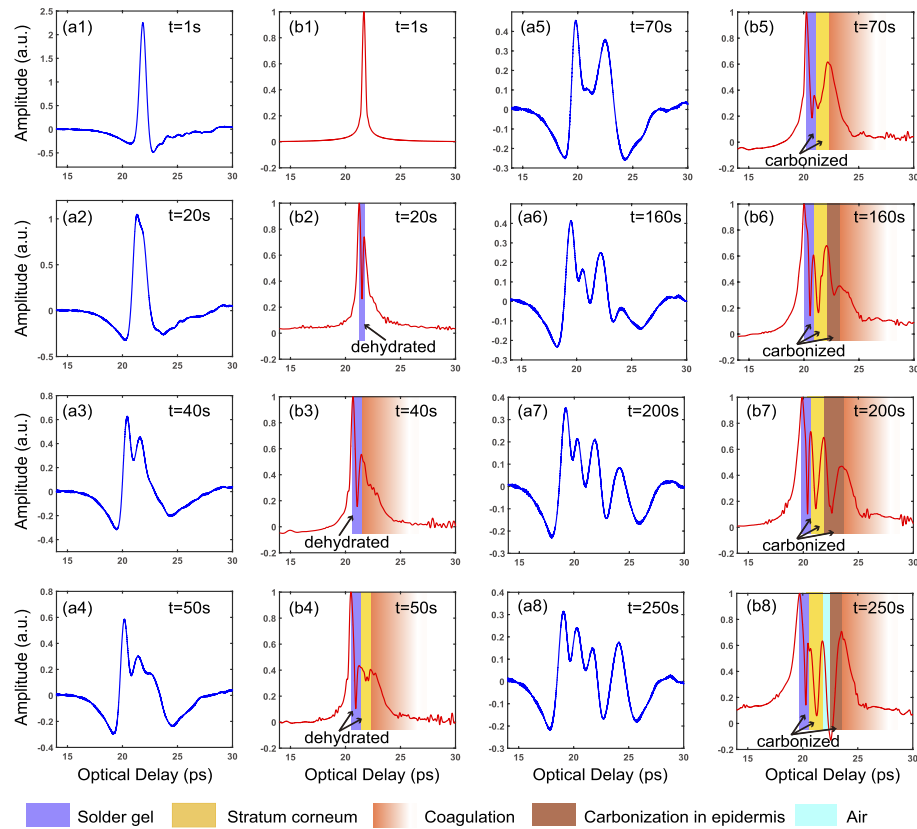


**Fig. 4.** Typical THz raw and deconvolved signals at specific time  $t$  from the dynamic THz single-point measurement. (a1-a8) correspond to the raw THz signals recorded at  $t = 1$  s, 20 s, 40 s, 50 s, 70 s, 160 s, 200 s and 250 s, respectively. (b1-b8) correspond to the deconvolved signals after applying the FWDD algorithm to the raw THz signals ranging from (a1) to (a8). Note that the deconvolved signals are normalized to their maximum peaks.

Based on the analysis above, we conclude that the deconvolved signal is able to reveal the evolution of the thermally-affected regions in both the solder and skin during plasmonic heating. Two strongly correlating indicators, the temporal duration and the number of peaks of the deconvolved signals, are identified to evaluate the thermally-affected regions. Translating from the optical delay to depth requires the knowledge of the refractive indices of the various zones. For instance, in Fig. 4(b2), the optical delay between the two peaks is 0.75 ps. Consequently, with the knowledge of the refractive index of BSA at 107 °C, which is about 1.80 [35], the thickness of the dehydrated solder layer can be estimated to be 44.20  $\mu\text{m}$ . Unfortunately, the refractive indices of skin under different damage levels in the THz regime are difficult to retrieve and are not yet available in literature. As previously mentioned, the refractive index of skin is highly dependent on its hydration level. When the skin is heated up to 100 °C, it starts to be dehydrated due to water evaporation until carbonization occurs. In this study, we use an effective refractive index of 1.20 [36], corresponding to dehydrated porcine skin, in order to estimate the depth of the thermal damage. Based on the deconvolved signal in Fig. 4(b8), such depth is estimated to be 315.30  $\mu\text{m}$ , considering a temporal delay of 5.35 ps. We would like to note that THz waves cannot penetrate into the coagulation zone, because of the local increase in water concentration [21]. Therefore, the depth of the thermal damage estimated in this study mainly corresponds to the thickness of the damage above the coagulation zone.

### 3.3. THz three-dimensional characterization of nanoparticle-assisted laser-tissue soldering

In this section, *in-vitro* experiments for nanoparticle-assisted laser soldering of an incision in the skin were performed and THz reflective imaging was conducted to quantitatively characterize the resulting thermal damage in three dimensions. A 5-mm-deep, 10-mm-long incision was made on the surface of porcine skin samples (dimension: 2.5 cm  $\times$  2 cm) using a surgical blade, following which the solder gel was applied onto both the center and the edges of the incision. This time, the same NIR laser featuring a focusing beam and spot size of 1.1 mm<sup>2</sup> was applied to the skin in order to achieve a rapid soldering. When a focusing laser beam is used, the thermally-affected region is expected to be limited to the incision and/or solder region, and this, in turn, can potentially reduce thermal damage of the peripheral tissue [37]. The skin sample was positioned onto a motorized translation stage, and the edges of the incision were brought into contact during the soldering. By moving the stage, the laser soldered the entire incision area (the length of which was 12 mm) by passing over it three consecutive times with a speed of 0.075 mm/s, each time with a small offset in the Y direction to ensure a broad solder line. The entire soldering procedure lasted 8 minutes and led to a strong skin tissue bonding effect. Three samples were prepared, and soldered with a laser intensity of 200 mW/mm<sup>2</sup>, 300 mW/mm<sup>2</sup>, and 400 mW/mm<sup>2</sup>. As the laser intensity increased, more regions featuring carbonization were observed on the surfaces of the samples, as shown in Fig. 5(a1-a3). It is worth mentioning that 200 mW/mm<sup>2</sup> is the minimum laser intensity found in our study to guarantee a satisfactory bonding strength. Following the laser soldering process, THz raster-scans with a spatial step of 0.5 mm were immediately conducted and 3D volume data were acquired for each sample. The FWDD algorithm was then applied to obtain the deconvolved signals, which were normalized to their maximum peak as previously done.

The THz in-plane images of soldered skin samples, obtained as two-dimensional presentations of the data and displayed as a top planar view of the samples, are shown in Fig. 5(b1-b3). The imaging contrast mechanism chosen here is the peak amplitude of the deconvolved THz signals, and each in-plane image is normalized to the maximum value of its pixels. The soldered regions in the center of the skin clearly feature lower contrast, since heat-induced variations of water content serve as the dominant contrast mechanism. While a THz in-plane image is an X-Y representation of the sample, a THz cross-sectional image provides depth information, along a

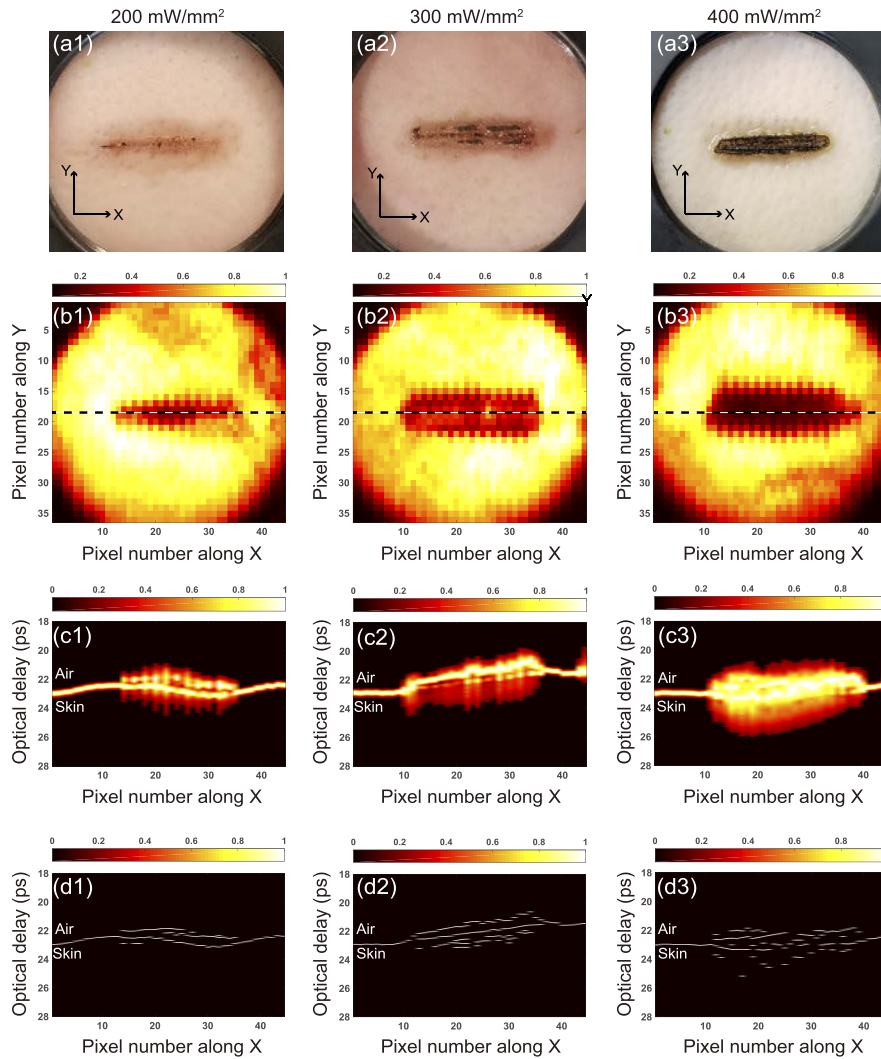


**Fig. 5.** THz imaging of porcine skin samples after nanoparticle-assisted laser soldering. (a1-a3) Digital photographs, (b1-b3) THz in-plane images, (c1-c3) THz cross-sectional images, and (d1-d3) binary THz cross-sectional images of the porcine skin samples after laser soldering with intensities of 200 mW/mm<sup>2</sup>, 300 mW/mm<sup>2</sup>, and 400 mW/mm<sup>2</sup>, respectively.

line in the X-Y plane. The temporal duration and the number of peaks of the deconvolved signals, the two indicators associated with the photothermal damage as a function of skin depth, can serve as the contrast mechanisms for the THz cross-sectional images. Such images, taken along the center of the soldered sites, are shown in Fig. 5(c1-c3). The imaging contrast mechanism chosen is simply the magnitude of the normalized deconvolved signals at a given optical delay. A threshold with a magnitude of 0.3 is set to remove the noise. In this way, THz cross-sectional images show the temporal duration (the first indicator) of each deconvolved signal along a line in the X-Y plane and, therefore, provide the depth information. By performing a peak-detection, binary THz cross-sectional images can be obtained. Here, the value '1' is assigned to a valid peak and the value '0' is instead assigned to the other positions regardless of the magnitude. Binary THz cross-sectional images, shown in Fig. 5(d1-d3), indicate the number of interfaces (the second indicator) detected along the depth. For a laser intensity of  $200 \text{ mW/mm}^2$ , both the air/solder and solder/skin interfaces are clearly observed in Fig. 5(c1). We note that the solder/skin interface reveals itself as a continuous line with a stronger contrast along the X direction. Our representation demonstrates that the solder gel was dehydrated by the laser-induced heat, and THz could thus reach the skin surface and penetrate the thermally-soldered region. However, the skin was not severely damaged, as shown in Fig. 5(d1), since an additional interface underneath the skin surface could only be detected within a small region. For a laser intensity of  $300 \text{ mW/mm}^2$ , the solder/skin interface features a weaker line compared to the previous case, indicating more THz penetration into the skin, as shown in Fig. 5(c2). Further, the longer temporal duration of the deconvolved signals demonstrates that the thermal-damaged regions shifted deeper into the skin. Additional interfaces below the skin surface were detected, presented in Fig. 5(d2), which demonstrate the existence of carbonization and coagulation zones in the skin. When the laser intensity reached  $400 \text{ mW/mm}^2$ , both the solder and the skin were severely burned, as clear interfaces can no longer be identified in Fig. 5(c3). The thermally-damaged region enlarged and moved further into the epidermis. As shown in Fig. 5(d3), more interfaces under the skin surface can be detected, indicating that a severe damage took place after soldering. Quantitative information on the depth of the thermal damage can be estimated from the THz cross-sectional images, upon the knowledge of the refractive index. Figure 6 illustrates the depth at which thermal damage occurred after laser soldering for each sample, based on the 3D volume data acquired via THz raster-scans. As it is possible to see, the most damaged area was always located along the soldered incision (which could reach about  $600 \mu\text{m}$  in depth for a laser density of  $400 \text{ mW/mm}^2$ ) and grew along both the radial and depth directions. These results clearly show how the thermal damage induced by laser soldering can be quantitatively characterized in three dimensions by means of the proposed technique.

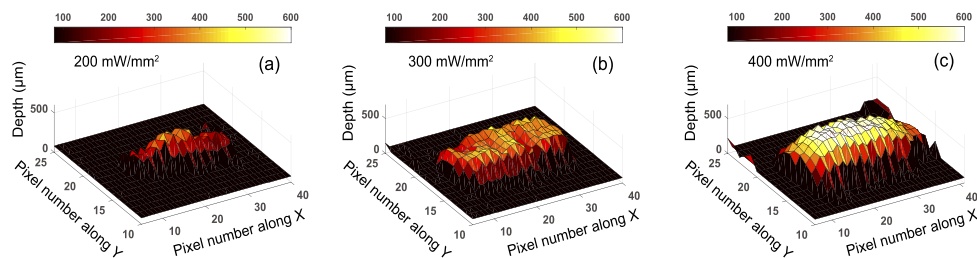


**Fig. 6.** THz three-dimensional images of the porcine skin samples after nanoparticle-assisted laser soldering with intensities of (a)  $200 \text{ mW/mm}^2$ , (b)  $300 \text{ mW/mm}^2$ , and (c)  $400 \text{ mW/mm}^2$ . The contrast mechanism is the estimated depth of the thermal damage induced by laser soldering.

#### 4. Conclusion

In conclusion, we have proposed a novel approach to perform simultaneous monitoring of nanoparticle-assisted laser-tissue interaction and 3D visualization of the photothermal damage induced by laser tissue soldering, taking advantage of the characteristic sensitivity of THz radiation to the water content in skin. We have demonstrated that the application of the GNR-embedded solder gel leads to a significant and well-confined increase of temperature in the treated area, thus enabling a rapid and strong soldering effect. However, during this process, the thermal gradient in the skin leads to the variation of its water content as a function of depth, resulting in the creation of different zones of thermal damage. By performing dynamic THz single-point measurements, the temporal evolution of THz signals associated with the resulting photothermal damage has been revealed, which provides a solid foundation for real-time monitoring of thermal dynamics in biological tissues with THz radiation. Moreover, *in-vitro* laser skin soldering experiments were conducted, and THz reflective imaging was utilized to quantitatively characterize the photothermal damage in three dimensions. Beyond the performed study, this approach can be considered as a versatile tool for further investigations into clinical therapies associated with laser-tissue interactions, such as tissue ablation and photothermal therapies.

#### Funding

Natural Sciences and Engineering Research Council of Canada; Canada Research Chairs; Fonds de recherche du Québec – Nature et technologies; Canada Foundation for Innovation; Mitacs; China Postdoctoral Science Foundation; National Key Research and Development Program of China; National Natural Science Foundation of China; Volkswagen Foundation.

#### Acknowledgments

We acknowledge our industrial partner TeTechS for the help offered at various stages of this project. We also would like to thank Prof. D. Ma and Prof. M.A. Gauthier for useful discussions. Note that R. Morandotti is affiliated to 2 as an adjunct faculty.

#### Disclosures

The authors declare no conflicts of interest.

#### References

1. S. H. Yun and S. J. J. Kwok, "Light in diagnosis, therapy and surgery," *Nat. Biomed. Eng.* **1**(1), 0008 (2017).
2. R. Schober, F. Ulrich, T. Sander, H. Dürselen, and S. Hessel, "Laser-induced alteration of collagen substructure allows microsurgical tissue welding," *Science* **232**(4756), 1421–1422 (1986).
3. L. S. Bass and M. R. Treat, "Laser tissue welding: A comprehensive review of current and future clinical applications," *Lasers Surg. Med.* **17**(4), 315–349 (1995).
4. P. Matteini, F. Rossi, L. Menabuoni, and R. Pini, "Microscopic characterization of collagen modifications induced by low-temperature diode-laser welding of corneal tissue," *Lasers Surg. Med.* **39**(7), 597–604 (2007).
5. R. A. White, R. Patrick Abergel, R. Lyons, S. R. Klein, G. Kopchok, R. M. Dwyer, and J. Uitto, "Biological effects of laser welding on vascular healing," *Lasers Surg. Med.* **6**(2), 137–141 (1986).
6. W. Happak, C. Neumayer, G. Holak, R. Kuzbari, G. Burgasser, and H. Gruber, "Morphometric and functional results after CO<sub>2</sub> laser welding of nerve coaptations," *Lasers Surg. Med.* **27**(1), 66–72 (2000).
7. S. Rose, A. Prevotau, P. Elzière, D. Hourdet, A. Marcellan, and L. Leibler, "Nanoparticle solutions as adhesives for gels and biological tissues," *Nature* **505**(7483), 382–385 (2014).
8. H. C. Huang, C. R. Walker, A. Nanda, and K. Rege, "Laser welding of ruptured intestinal tissue using plasmonic polypeptide nanocomposite solders," *ACS Nano* **7**(4), 2988–2998 (2013).
9. W. He, J. Frueh, N. Hu, L. Liu, M. Gai, and Q. He, "Guidable Thermophoretic Janus Micromotors Containing Gold Nanocolorifiers for Infrared Laser Assisted Tissue Welding," *Adv. Sci.* **3**(12), 1600206 (2016).
10. G. Baffou and R. Quidant, "Thermo-plasmonics: using metallic nanostructures as nano-sources of heat," *Laser Photonics Rev.* **7**(2), 171–187 (2013).



11. H. Breitenborn, J. Dong, R. Piccoli, A. Bruhacs, L. V. Besteiro, A. Skripka, Z. M. Wang, A. O. Govorov, L. Razzari, F. Vetrone, R. Naccache, and R. Morandotti, "Quantifying the photothermal conversion efficiency of plasmonic nanoparticles by means of terahertz radiation," *APL Photonics* **4**(12), 126106 (2019).
12. R. Anderson and J. Parrish, "Selective photothermolysis: precise microsurgery by selective absorption of pulsed radiation," *Science* **220**(4596), 524–527 (1983).
13. M. A. Ansari, M. Erfanzadeh, and E. Mohajerani, "Mechanisms of laser-tissue interaction: II. tissue thermal properties," *Journal of Lasers in Medical Sciences* **4**, 99–106 (2013).
14. P. Matteini, F. Ratto, F. Rossi, and R. Pini, "Emerging concepts of laser-activated nanoparticles for tissue bonding," *J. Biomed. Opt.* **17**(1), 010701 (2012).
15. M. Tonouchi, "Cutting-edge terahertz technology," *Nat. Photonics* **1**(2), 97–105 (2007).
16. E. Pickwell, B. E. Cole, A. J. Fitzgerald, M. Pepper, and V. P. Wallace, "In vivo study of human skin using pulsed terahertz radiation," *Phys. Med. Biol.* **49**(9), 1595–1607 (2004).
17. Z. D. Taylor, R. S. Singh, D. B. Bennett, P. Tewari, C. P. Kealey, N. Bajwa, M. O. Culjat, A. Stojadinovic, H. Lee, J. P. Hubschman, E. R. Brown, and W. S. Grundfest, "THz medical imaging: In vivo hydration sensing," *IEEE Trans. Terahertz Sci. Technol.* **1**(1), 201–219 (2011).
18. R. Naccache, A. Mazhorova, M. Clerici, R. Piccoli, L. K. Khorashad, A. O. Govorov, L. Razzari, F. Vetrone, and R. Morandotti, "Terahertz Thermometry: Combining Hyperspectral Imaging and Temperature Mapping at Terahertz Frequencies," *Laser Photonics Rev.* **11**(5), 1600342 (2017).
19. P. Jepsen, D. Cooke, and M. Koch, "Terahertz spectroscopy and imaging - Modern techniques and applications," *Laser Photonics Rev.* **5**(1), 124–166 (2011).
20. M. H. Arbab, T. C. Dickey, D. P. Winebrenner, A. Chen, M. B. Klein, and P. D. Mourad, "Terahertz reflectometry of burn wounds in a rat model," *Biomed. Opt. Express* **2**(8), 2339 (2011).
21. P. Tewari, C. P. Kealey, D. B. Bennett, N. Bajwa, K. S. Barnett, R. S. Singh, M. O. Culjat, A. Stojadinovic, W. S. Grundfest, and Z. D. Taylor, "In vivo terahertz imaging of rat skin burns," *J. Biomed. Opt.* **17**(4), 040503 (2012).
22. C. S. Joseph, R. Patel, V. A. Neel, R. H. Giles, and A. N. Yaroslavsky, "Imaging of ex vivo nonmelanoma skin cancers in the optical and terahertz spectral regions," *J. Biophotonics* **7**(5), 295–303 (2014).
23. R. M. Woodward, B. E. Cole, V. P. Wallace, R. J. Pye, D. D. Arnone, E. H. Linfield, and M. Pepper, "Terahertz pulse imaging in reflection geometry of human skin cancer and skin tissue," *Phys. Med. Biol.* **47**(21), 3853–3863 (2002).
24. T. Bowman, M. El-Shenawee, and L. K. Campbell, "Terahertz transmission vs reflection imaging and model-based characterization for excised breast carcinomas," *Biomed. Opt. Express* **7**(9), 3756 (2016).
25. S. Selvin, S. Sung, N. Bajwa, A. D. Li, Z. D. Taylor, E. R. Brown, B. Nowroozi, W. S. Grundfest, S. X. Deng, J. Goell, J. Garritano, and S. Chandra, "THz Imaging System for *in vivo* Human Cornea," *IEEE Trans. Terahertz Sci. Technol.* **8**(1), 27–37 (2018).
26. G. G. Hernandez-Cardoso, S. C. Rojas-Landeros, M. Alfaro-Gomez, A. I. Hernandez-Serrano, I. Salas-Gutierrez, E. Lemus-Bedolla, A. R. Castillo-Guzman, H. L. Lopez-Lemus, and E. Castro-Camus, "Terahertz imaging for early screening of diabetic foot syndrome: A proof of concept," *Sci. Rep.* **7**(1), 42124 (2017).
27. O. A. Smolyanskaya, I. J. Schelkanova, M. S. Kulya, E. L. Odlyanitskiy, I. S. Goryachev, A. N. Tcypkin, Y. V. Grachev, Y. G. Toropova, and V. V. Tuchin, "Glycerol dehydration of native and diabetic animal tissues studied by THz-TDS and NMR methods," *Biomed. Opt. Express* **9**(3), 1198 (2018).
28. U. Jacobi, M. Kaiser, R. Toll, S. Mangelsdorf, H. Audring, N. Otberg, W. Sterry, and J. Lademann, "Porcine ear skin: An in vitro model for human skin," *Skin Research and Technol.* **13**(1), 19–24 (2007).
29. M. Mushaben, R. Urie, T. Flake, M. Jaffe, K. Rege, and J. Heys, "Spatiotemporal modeling of laser tissue soldering using photothermal nanocomposites," *Lasers Surg. Med.* **50**(2), 143–152 (2018).
30. K. M. McNally, B. S. Sorg, N. C. Bhavaraju, M. G. Ducros, A. J. Welch, and J. M. Dawes, "Optical and thermal characterization of albumin protein solders," *Appl. Opt.* **38**(31), 6661 (1999).
31. Y. Ren, H. Qi, Q. Chen, and L. Ruan, "Thermal dosage investigation for optimal temperature distribution in gold nanoparticle enhanced photothermal therapy," *Int. J. Heat Mass Transfer* **106**, 212–221 (2017).
32. J. Dong, J. Bianca Jackson, M. Melis, D. Giovanacci, G. C. Walker, A. Locquet, J. W. Bowen, and D. S. Citrin, "Terahertz frequency-wavelet domain deconvolution for stratigraphic and subsurface investigation of art painting," *Opt. Express* **24**(23), 26972 (2016).
33. J. Dong, A. Locquet, and D. S. Citrin, "Depth resolution enhancement of terahertz deconvolution by autoregressive spectral extrapolation," *Opt. Lett.* **42**(9), 1828 (2017).
34. J. Dong, A. Locquet, and D. S. Citrin, "Enhanced Terahertz Imaging of Small Forced Delamination in Woven Glass Fibre-reinforced Composites with Wavelet De-noising," *J. Infrared, Millimeter, Terahertz Waves* **37**(3), 289–301 (2016).
35. X. Li, X. Fu, J. Liu, Y. Du, and Z. Hong, "Investigation of thermal denaturation of solid bovine serum albumin by terahertz dielectric spectroscopy," *J. Mol. Struct.* **1049**, 441–445 (2013).
36. D. B. Bennett, W. Li, Z. D. Taylor, W. S. Grundfest, and E. R. Brown, "Stratified media model for terahertz reflectometry of the skin," *IEEE Sens. J.* **11**(5), 1253–1262 (2011).
37. J. Jiao and Z. Guo, "Thermal interaction of short-pulsed laser focused beams with skin tissues," *Phys. Med. Biol.* **54**(13), 4225–4241 (2009).